Journal of Energy Chemistry 111 (2025) 288–296

Contents lists available at ScienceDirect

Journal of Energy Chemistry

journal homepage: www.elsevier.com/locate/jechem

http://www.journals.elsevier.com/journal-of-energy-chemistry/

Enhancement of hydrogen-bond network connectivity and CO poisoning resistance via Mn-mediated electron transfer

Chenggong Niu [a], Linyu Chen [a], Yi Liu [a], Shuqing Zhou [a], Heyang Liu [a], Tingting Tang [a], Jingya Guo [a,*], Tayirjan Taylor Isimjan [b,*], Xiulin Yang [a,*]

[a] Guangxi Key Laboratory of Low Carbon Energy Materials, School of Chemistry and Pharmaceutical Sciences, Guangxi Normal University, Guilin 541004, Guangxi, China
[b] Saudi Arabia Basic Industries Corporation (SABIC) at King Abdullah University of Science and Technology (KAUST), Thuwal 23955-6900, Saudi Arabia

ARTICLE INFO

Article history:
Received 15 May 2025
Revised 23 July 2025
Accepted 29 July 2025
Available online 7 August 2025

Keywords:
Oxyphilic metals
Hydrogen oxidation reaction
Electronic regulation
Hydrogen-bond network
CO-resilient

ABSTRACT

The strategic incorporation of oxyphilic metals to precisely regulate Pt-based electronic structures emerges as a promising approach for boosting alkaline hydrogen oxidation reaction (HOR) activity and CO poisoning resistance. Herein, we successfully prepare the Mn/Pt-PtS catalyst, which exhibits a linear structure composed of stacked nanoparticles. The Mn integration simultaneously enhances charge transfer kinetics and electrical conductivity while optimizing reaction dynamics. In situ attenuated total reflection surface-enhanced infrared absorption spectroscopy (ATR-SEIRAS) characterization further demonstrates that Mn incorporation facilitates the establishment of enhanced hydrogen-bond networks, thereby promoting HOR processes. Remarkably, the Mn/Pt-PtS catalyst achieves exceptional performance with a $j_{0,s}$ of 1.95 mA cm^{-2} and maintains robust CO tolerance even under 1000 ppm CO exposure. Combined experimental and theoretical analyses reveal synergistic electronic interactions within the catalyst system, which induce *d*-band center downshifting, optimize intermediate adsorption strength, and reduce reaction energy barriers.

1. Introduction

Hydrogen (H_2) energy is recognized as a powerful alternative to fossil fuels due to its high energy density, sustainability, and eco-friendliness, effectively alleviating the global energy and environmental crisis [1,2]. Anion exchange membrane fuel cells (AEMFCs) are particularly advantageous for their capability to convert clean, high-energy hydrogen fuel directly into electricity in an alkaline environment [2,3]. However, the kinetics of anodic hydrogen oxidation reaction (HOR) in AEMFCs experiences a considerable decline when transitioning from acidic to alkaline conditions [4]. Furthermore, steam reforming of natural gas remains the primary economically feasible method for hydrogen production, inevitably introducing CO gas and resulting in the generation of grey hydrogen [5,6]. The catalysts are susceptible to CO poisoning, even at ppm levels, which compromises their electrocatalytic efficiency [5,7]. Therefore, the development of economical alkaline HOR catalysts with high performance and superior resistance to CO poisoning is essential for advancing AEMFC technology.

Non-noble metal catalysts show low stability and catalytic activity due to high hydrogen binding energy [2]. Platinum (Pt) has been extensively utilized as a HOR catalyst due to its near-optimal hydrogen binding strength [2,5,8]. Nevertheless, these catalysts are prone to CO poisoning at ppm concentrations, which diminishes their electrocatalytic activity [5,9]. To enhance the efficacy of Pt-based catalysts, researchers have explored various strategies, including doping, heterostructure engineering, and alloying, aimed at improving HOR activity, bolstering resistance to poisoning, and extending stability [10–12]. Recent advancements in in-situ characterizations have identified OH_{ad} species during the alkaline HOR process, which are crucial for determining catalytic activity [13]. Studies indicate that the introduction of oxyphilic metal atoms can lower the *d*-band center, weaken the binding strengths of *H and *CO, and enhance OH adsorption, thus accelerating the Volmer step via a bifunctional mechanism [5,10,14]. For instance, Huang et al. proposed a universal strategy of integrating oxyphilic metal atoms into PtRu nanowires (designated as i-M-PR), leading to improved HOR activity and CO

* Corresponding authors.
E-mail addresses: jyguo@gxnu.edu.cn (J. Guo), isimjant@sabic.com (T.T. Isimjan), xlyang@gxnu.edu.cn (X. Yang).

https://doi.org/10.1016/j.jechem.2025.07.070

poisoning resistance [14]. Consequently, it is anticipated that the incorporation of oxyphilic metal atoms will effectively enhance the HOR activity and CO tolerance of Pt-based catalysts. Compared with other oxophilic metals, metallic Mn effectively increases the electrochemical surface area, exposes more active sites, and improves catalyst stability [10,14–16].

In this work, by introducing the oxophilic metal Mn, we prepared a linear structure composed of stacked Mn/Pt-PtS nanoparticles. This unique linear structure featured abundant interfaces, yielding a larger specific surface area and exposing more active sites. As predicted, the resulting Mn/Pt-PtS catalyst exhibited excellent catalytic performance in the alkaline HOR. Additionally, Mn/Pt-PtS demonstrated remarkable long-term stability and remarkable CO poisoning resistance. Density functional theory (DFT) calculations elucidated the electronic interactions within the Mn/Pt-PtS catalyst. This behavior caused a shift in the *d*-band center, optimizing the adsorption strength of intermediates and lowering the energy barrier for the HOR. In-situ ATR-SEIRAS results confirmed that the incorporation of Mn effectively encouraged the formation of a robust hydrogen-bond network, significantly enhancing the alkaline HOR activity by accelerating the Volmer step.

2. Experimental

2.1. Chemicals

All chemicals and reagents were utilized as purchased without any further purification. These chemicals and reagents included manganese (II) chloride tetrahydrate ($MnCl_2{\cdot}4H_2O$, ≥99.0 %), hydrogen hexachloroplatinate (IV) ($H_2PtCl_6{\cdot}6H_2O$, Pt ≥37.5 %), sodium sulfide ($Na_2S{\cdot}9H_2O$, ≥98.0 %), ethanol absolute (C_2H_5OH, 99.7 %), commercial Pt/C (20 wt% Pt), nafion solution (5 wt%), and potassium hydroxide (KOH, >95 %). The deionized water (18.25 MΩ cm^{-1}) from a water purification system (Ulupure) was used throughout the whole experiment.

2.2. Synthesis of Mn/Pt-PtS and Pt-PtS

Taking the optimal synthesis method for Mn/Pt-PtS as an example, 0.04 mmol $H_2PtCl_6{\cdot}6H_2O$, 0.12 mmol $Na_2S{\cdot}9H_2O$, and 0.15 mmol $MnCl_2{\cdot}4H_2O$ were quickly mixed in a beaker containing 15 mL DI water and 15 mL ethanol, and stirred for another 20 min at room temperature. The mixture was stirred for an additional 20 min at room temperature before being transferred to a 100 mL Teflon-lined autoclave, where it was heated to 180 °C for 24 h. The resultant precursors were harvested by centrifugation, washed several times with ethanol, and then dried overnight in a vacuum oven. The precursor was then annealed at 350 °C for 2 h at a heating rate of 5 °C min^{-1} in N_2 atmosphere. After naturally cooling, the obtained sample was denoted as Mn/Pt-PtS.

As a control, the synthesis of Pt-PtS followed a similar procedure to that of Mn/Pt-PtS, but without the addition of the Mn source.

2.3. Materials characterization

Powder X-ray diffraction (XRD, Rigaku D/Max 2500V/PC, Japan, Cu K_α radiation over the 2θ range of 10°–90°) was measured to investigate the crystal structure and phase composition of samples. Scanning electron microscopy (SEM, FEI Quanta 200 FEG) and transmission electron microscopy (TEM, JEM-2100 F) were used to characterize the morphology and elemental distribution of the catalysts. The chemical state and electronic structure of the samples were analyzed by X-ray photoelectron spectroscopy (XPS, JPS-9010 Mg K_α). Metal contents in the catalysts were examined using inductively coupled plasma mass spectroscopy (ICP-MS, PerkinElmer corporation, FLexar-NexION300X). The specific Brunauer-Emmett-Teller (BET) surface area and pore size distribution of the samples were measured. Ultraviolet photoelectron spectroscopy (UPS) was performed on X-ray photoelectron spectroscopy (PHI5000 VersaProbe III).

2.4. Electrochemical characterization

The electrochemical measurements were performed in a three-electrode system using a CHI 760E (Shanghai, China) electrochemical workstation at room temperature. A rotating disk electrode (RDE, PINE, 5.00 mm diameter, disk area: 0.196 cm^2) with glassy carbon served as the working electrode, the Ag/AgCl electrode was applied as a reference electrode, and a carbon rod was used as a counter electrode, respectively. All potentials were converted to the reversible hydrogen electrode (RHE) scale via calibration. The RHE calibration was performed in high-purity H_2-saturated 0.1 M KOH with a Pt foil as the working electrode ($E_{Ag/AgCl}$ + 0.19 7 + 0.059 × pH).

2.5. Hydrogen oxidation reaction (HOR) measurements

Bubbling was performed for 30 min to achieve H_2 saturation. The electrode was pre-cycled between 0 and 1.0 V (vs. RHE) in pre-prepared N_2-saturated 0.1 M KOH to reach a steady state. HOR polarization curves were collected at a rotation speed of 1600 r min^{-1} using a RDE with a scan rate of 10 mV s^{-1}, in the range from 0.05 to 0.5 V (vs. RHE).

To prepare the working electrode, 3 mg of the sample and 5 μL of Nafion solution (5 wt%) were ultrasonically dispersed in deionized water-isopropanol solution (volume ratio of 1:1) to form a homogeneous ink. Afterwards, 15 μL of well-dispersed catalyst ink was suspended onto the pre-polished glassy carbon electrode, and the ink was dried prior to measurement. The catalyst loading was 0.093 mg_{Pt} cm^{-2}, which was calculated by ICP-MS data.

3. Results and discussion

3.1. Synthesis and structural analysis

Fig. 1(a) depicts the synthetic route for Mn/Pt-PtS, achieved through hydrothermal and carbonization approaches. Specifically, H_2PtCl_6 precursor, $MnCl_2$, and Na_2S were first ultrasonically dissolved in a solvent mixture of ethanol and water. The precursors were then synthesized using a direct hydrothermal method. Eventually, the samples obtained from the hydrothermal process were annealed under a nitrogen atmosphere to yield the Mn/Pt-PtS catalysts. SEM and TEM served as effective tools for examining the microstructure of the electrocatalysts. As depicted in Fig. S1, the catalyst without the Mn source appeared as irregular blocky solids with noticeable agglomeration. In contrast, the introduction of the Mn source altered the morphology of Mn/Pt-PtS into linear structures formed by nanoparticle accumulation. These structures are characterized by numerous interfaces, stepped atomic surfaces, and reactive unsaturated sites, which significantly enhance the alkaline HOR performance of Mn/Pt-PtS (Fig. 1b and Fig. S2) [17]. In addition, by adjusting different Mn contents, we found that an appropriate amount of Mn could effectively reduce the agglomeration of the catalyst, which might be one of the reasons affecting the HOR performance (Fig. S3). Fig. 1(c) confirmed that Mn/Pt-PtS was a nanowire structure composed of sheets, consisting of nanoparticles with an average size of approximately 11.73 nm. To further assess the thickness of the sample, atomic force

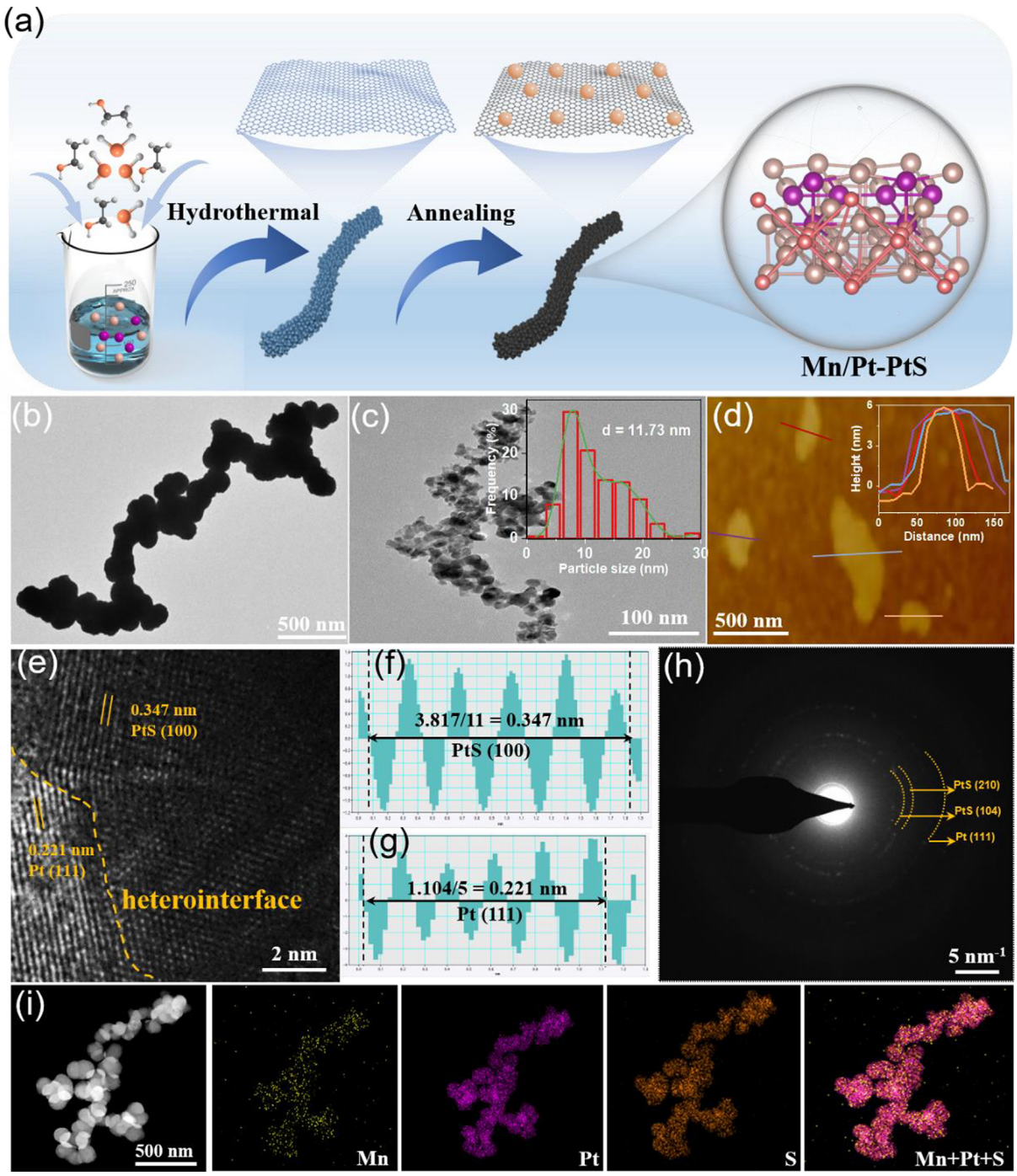

Fig. 1. (a) Scheme for the synthesis of Mn/Pt-PtS. (b) TEM image of Mn/Pt-PtS. (c) TEM image and the particle size distribution (inset) of Mn/Pt-PtS. (d) AFM image of the Mn/Pt-PtS flakes (the inset shows the corresponding line-trace height profile across flakes). (e–g) High-resolution TEM images of Mn/Pt-PtS. (h) SAED pattern of Mn/Pt-PtS. (i) Elemental mappings of Mn/Pt-PtS.

microscopy (AFM) was utilized, revealing that Mn/Pt-PtS maintained a thickness of approximately 6.0 nm (Fig. 1d).

The interface of Mn/Pt-PtS was clearly visible in Fig. 1(e), where the Pt (111) crystal plane and PtS (100) crystal plane are present (the heterointerfaces are indicated by yellow dashed lines). Analysis combining Fig. 1(e–g) and Fig. S4 showed that the lattice fringe spacings of PtS (100) and Pt (111) planes in Pt-PtS were 0.347 and 0.215 nm, respectively. In sharp contrast, for Mn/Pt-PtS, the lattice fringe spacing of the PtS (100) plane remained at 0.347 nm, while that of the Pt (111) plane increased to 0.221 nm. This change indicated that the introduction of Mn significantly altered the lattice fringe spacing of the Pt (111) plane, confirming the successful incorporation of Mn atoms into the Pt lattice [14]. Furthermore, the selected area electron diffraction (SAED) pattern indicated a sequence of diffraction rings corresponding to the (210) and (104) planes of PtS and the (111) plane of Pt (Fig. 1h). As exhibited in Fig. 1(i), the high-angle annular dark-field scanning TEM (HAADF-STEM)-energy dispersive X-ray spectroscopy mappings indicated the coexistence of Mn, S, and Pt elements throughout the whole heterostructure.

The crystallographic texture of the obtained catalysts was elucidated by XRD patterns. As shown in Fig. 2(a), the diffraction peaks

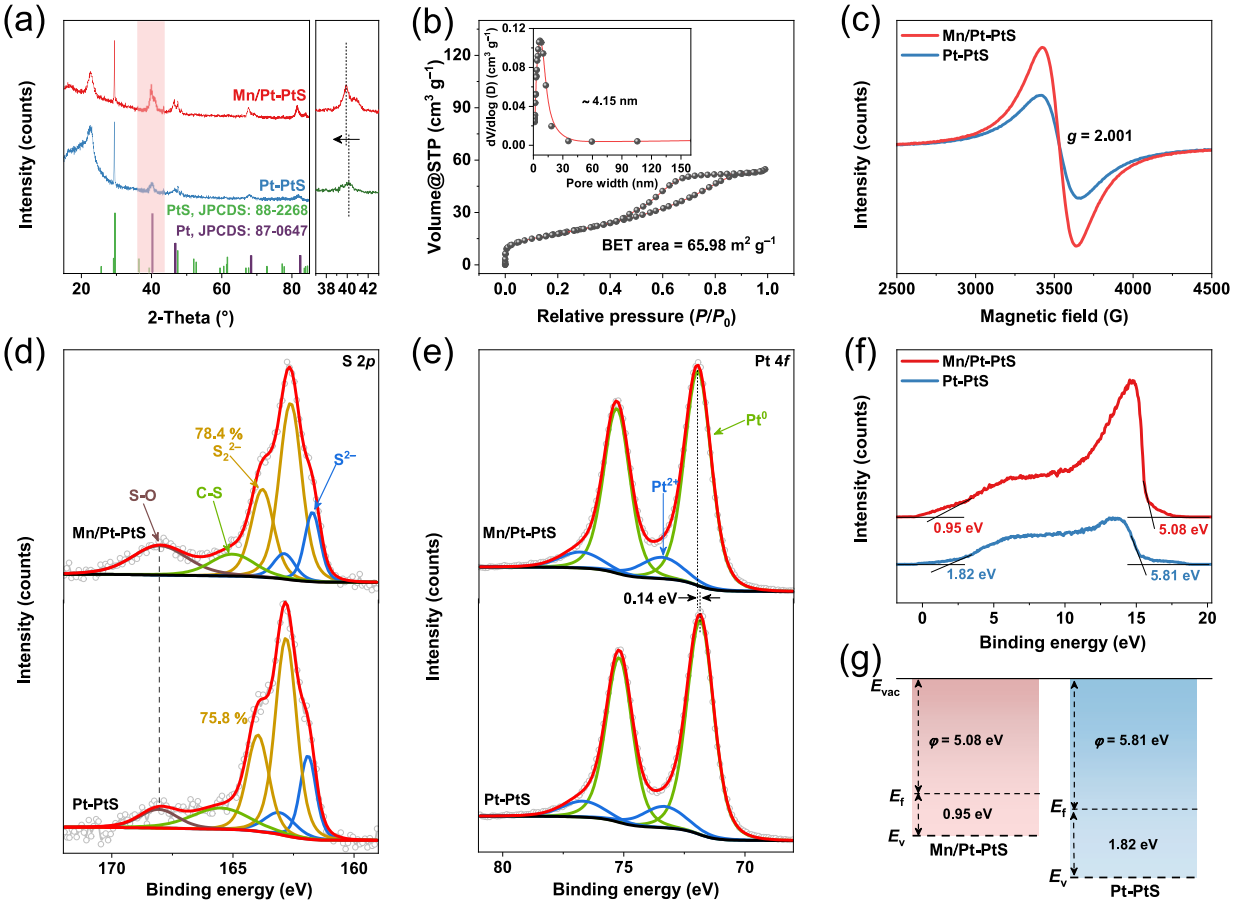

Fig. 2. (a) XRD patterns of Mn/Pt-PtS and Pt-PtS. (b) N_2 adsorption-desorption isotherms and pore size distribution (inset) of Mn/Pt-PtS. (c) EPR spectra of Mn/Pt-PtS and Pt-PtS. High-resolution (d) S 2*p* and (e) Pt 4*f* XPS spectra in Mn/Pt-PtS and Pt-PtS. (f) UPS spectra and (g) band structure alignment of Mn/Pt-PtS and Pt-PtS.

for Mn/Pt-PtS and Pt-PtS correspond to the PtS (JCPDS: 88-2268) and Pt phases (JCPDS: 87-0647), respectively. It is worth noting that the Pt (111) crystal plane of Mn/Pt-PtS exhibits a negative shift compared to Pt-PtS, suggesting a slight expansion of its lattice. This observation is consistent with the finding that the lattice spacing of Pt increased [18]. Analysis of the BET adsorption-desorption isotherm determined that the specific surface area of Mn/Pt-PtS was 65.98 $m^2\ g^{-1}$. The pore size distribution of Mn/Pt-PtS predominantly appeared as a mesoporous structure with an average pore size of 4.15 nm (Fig. 2b) [4]. The high specific surface area and mesoporous structure of Mn/Pt-PtS enabled balanced electrolyte permeation and ionic diffusion, resulting in expediting the reaction kinetics [19,20]. Additionally, electron paramagnetic resonance (EPR) detected a significant signal for unpaired electrons at g = 2.001, suggesting a rich presence of sulfur vacancies in Mn/Pt-PtS and Pt-PtS catalysts (Fig. 2c) [21]. Abundant sulfur vacancies had unique advantages in promoting the HOR catalytic activity, echoing previous reports [21,22].

XPS was conducted to elucidate the surface composition and chemical states of the samples [23]. The S 2*p* spectra show four distinct components corresponding to S^{2-} (161.77 eV), S_2^{2-} (162.64 eV), C–S (165.07 eV), and S–O bonds (168.05 eV), which align well with previously reported literature (Fig. 2d) [24,25]. Moreover, through the analysis of the ratio of fitted peak areas, we investigated the relationship between the content of S_2^{2-} and the intensity of sulfur vacancies. We found that the content of S_2^{2-} correlates with the intensity of sulfur vacancies, indicating a close connection between the formation of S_2^{2-} and sulfur vacancies [26]. To further assess the impact of Mn incorporation, high-resolution Pt 4*f* spectra were analyzed. As shown in Fig. 2 (e), the peaks at 71.73 and 75.18 eV are attributed to Pt^0, while those at 73.35 and 76.70 eV correspond to Pt^{2+} [10]. The Pt^0 peak in Mn/Pt-PtS shifts positively compared to Pt-PtS, indicating that the atomically dispersed Mn dopant interacts electronically with the Pt matrix, modifying its electronic distribution and demonstrating the electronic modulation capability of the Mn dopant [10]. Additionally, no distinct peaks for the Mn 2*p* orbitals were detected, likely due to the relatively low Mn content (Fig. S5). Therefore, we tested the sample with the highest Mn content using XPS. The Mn 2*p* spectrum could be deconvoluted into two pairs of peaks, corresponding to Mn^{2+} (637.94 eV) and Mn^{3+} (641.35 eV), which allowed us to roughly determine the oxidation states of Mn (Fig. S5) [27]. UPS measurements revealed significant differences in work function (WF) before and after Mn incorporation. As depicted in Fig. 2(f, g), the WF trend was Mn/Pt-PtS (5.08 eV) < Pt-PtS (5.81 eV), indicating that the doping of Mn facilitated easier electron transfer from the interior of the catalyst to its surface, thereby enabling faster reaction kinetics through electron exchange with reactants [28]. The maximum valence band values for Mn/Pt-PtS and Pt-PtS were 0.95 and 1.82 eV, respectively. Obviously, the incorporation of Mn into Pt-PtS brought the valence band closer to the Fermi level (E_f), suggesting that Mn/Pt-PtS exhibited better conductivity [29].

3.2. Electrochemical HOR performance

The electrocatalytic HOR performance of the synthesized catalysts was examined utilizing a RDE system in a standard three-

electrode setup within 0.1 M H_2-saturated KOH electrolyte. The optimal synthesis parameters were determined by varying the temperature and the Mn doping levels. The Mn/Pt-PtS catalyst, synthesized at a carbonation temperature of 350 °C with 2.95 % of Mn, demonstrated peak HOR activity (Fig. S6 and Table S1). Linear sweep voltammetry revealed that Mn/Pt-PtS achieved the highest anodic current density across the entire potential range, outperforming both Pt-PtS and Pt/C. Control experiments in N_2-saturated electrolyte confirmed that the anodic current primarily originated from H_2 oxidation rather than other substances (Fig. 3a and Fig. S7) [1]. Rotational speed-dependent polarization curves of Mn/Pt-PtS demonstrated mass-transfer-controlled H_2 oxidation characteristics, with limiting current densities showing positive correlation with rotation rates [30]. The Koutecky-Levich plot created at 50 mV (inset of Fig. 3b, Figs. S8, and S9) demonstrated a linear relationship between the inverse of the total current density and the square root of the rotation speed, which closely matches the theoretical value for the two-electron transfer HOR process (4.71 cm^2 mA^{-1} $r^{-1/2}$ $min^{1/2}$) [17]. Furthermore, we confirmed the catalytic mechanism of the HOR via Tafel slope analysis (Fig. 3c), where the asymmetric behavior in the Tafel plot indicated that Mn/Pt-PtS followed the Heyrovsky-Volmer mechanism, with the Volmer step acting as the rate-determining step [1]. In Fig. 3(d), the value of exchange current density (j_0) for the sample was derived from linear fitting in the micro-polarization region (from –5 to 5 mV). The j_0 of Mn/Pt-PtS was 2.19 mA cm^{-2}, demonstrating good intrinsic activity for HOR compared to other catalysts (Fig. 3e). Furthermore, electrochemical impedance spectroscopy (EIS) was used to evaluate the charge transfer capability. As shown in Fig. S10, Mn/Pt-PtS exhibited a lower charge transfer resistance, indicating faster charge transfer and better conductivity [31,32]. Recent findings by Luo et al. highlighted that S sites play a critical role in enhancing HOR activity, as demonstrated by S-site blocking experiments [21]. The role of S sites can be effectively verified through S-site blocking experiments, where Zn^{2+} binds to S sites, hindering the adsorption of H and thus reducing catalytic activity. Relevant experiments are shown in Fig. 3(f). After introducing Zn^{2+}, the HOR performance of Mn/Pt-PtS decreased significantly, suggesting that S sites are crucial for enhancing its electrochemical performance. To verify the toxic effect of Zn^{2+} on the catalyst itself, we conducted a control experiment using Pt/C. As shown in Fig. S11, the catalytic activity of Pt/C decreased to a lesser extent, further confirming that Zn^{2+} primarily functions by binding to S sites. Moreover, when no S element was added, the catalytic activity of Pt/Mn was much lower than that of Mn/Pt-PtS and Pt-PtS. This further supports the idea that S sites play a key role in enhancing HOR performance (Fig. S12). Simultaneously, the specific activities ($j_{0,s}$) and mass activity (MA) of Mn/Pt-PtS exceeded those of most recorded Pt-based catalysts (Fig. 3g and Tables S2–S4). Moreover, the long-term stability of the catalyst was assessed using

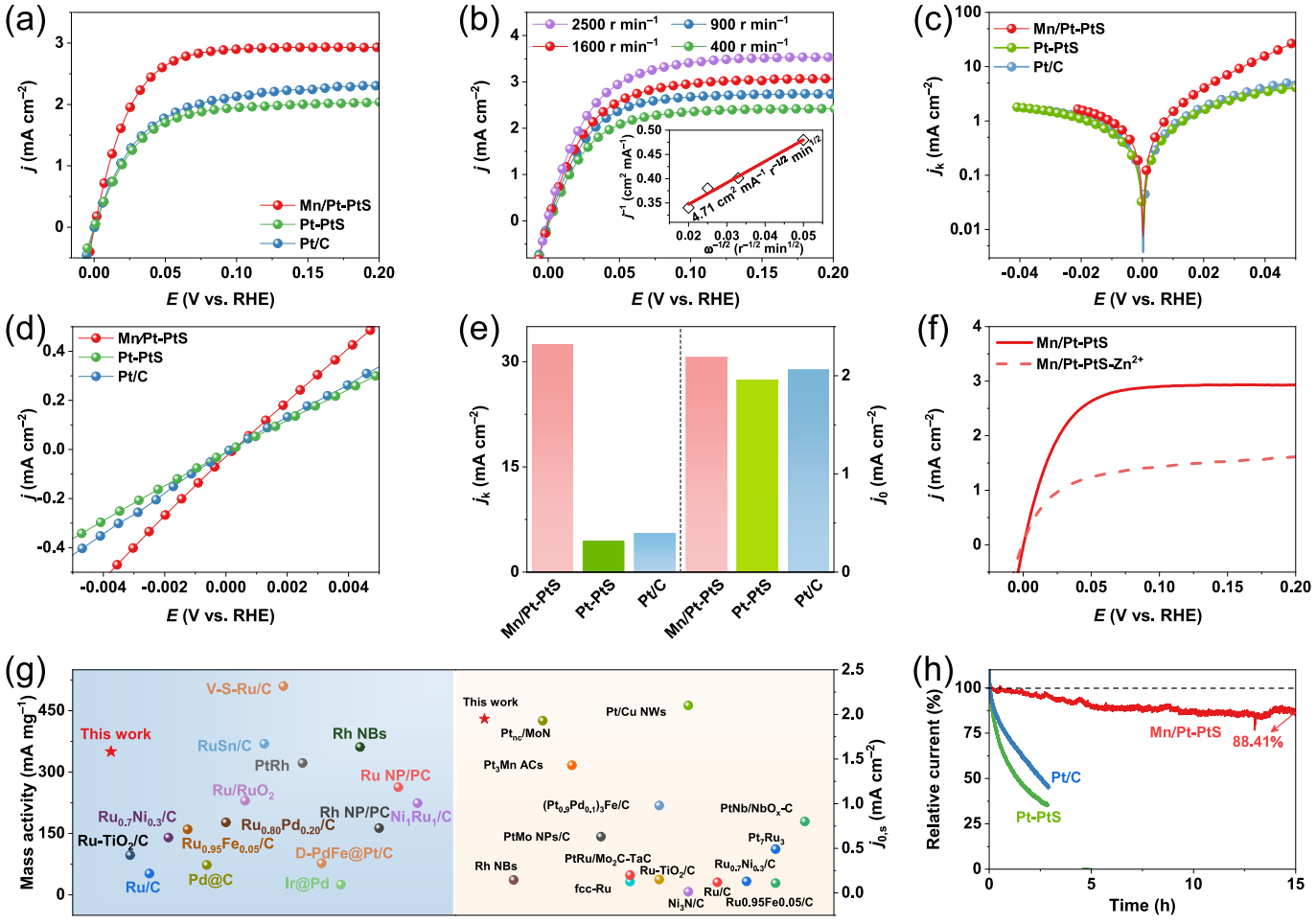

Fig. 3. (a) HOR polarization curves of Mn/Pt-PtS, Pt-PtS, and commercial Pt/C. (b) HOR polarization curves for Mn/Pt-PtS at various rotation speeds. Inset shows the corresponding Koutecky-Levich plots at 50 mV. (c) Tafel plots. (d) Linear fitting curves in the micropolarization region. (e) Comparison of j_k and j_0 of studied electrocatalysts. (f) HOR polarization curves of Mn/Pt-PtS before and after soaking in 1 mM $Zn(NO_3)_2$ solution for 30 s. (g) $j_{0,s}$ and MA of Mn/Pt-PtS compared to other recently reported alkaline HOR electrocatalysts. (h) Chronoamperometric (j-t) responses at 50 mV for Mn/Pt-PtS and commercial Pt/C.

chronoamperometry in a 0.1 M KOH electrolyte. As performed in Fig. 3(h), after operating for 54,000 s, Mn/Pt-PtS maintained a current retention rate of 88 %, whereas Pt/C and Pt-PtS exhibited a significant decline after 9000 s, confirming the exceptional long-term stability of Mn/Pt-PtS for the HOR. Furthermore, we collected the samples after the reaction for testing. As shown in Fig. S13, after the long-term reaction, the Pt (200) crystal plane and PtS (101) crystal plane are clearly visible (dashed lines indicate heterointerfaces). XRD analysis revealed that the structure of the material did not change significantly after the reaction, indicating the stability of the material structure (Fig. S14). Meanwhile, XPS results showed that the valence states of S and Pt remained almost unchanged after the long-term test, which further illustrated the stability of the material structure (Fig. S15). Furthermore, it was found that the dissolution amount of Mn was approximately 39 ppm after long-term stability tests.

3.3. In situ ATR-SEIRAS analysis and CO-tolerance evaluation

The binding energies of H_{ad} and OH_{ad} species on the electrocatalyst surfaces exhibited strong correlations with hydrogen electrocatalytic activity in alkaline media [33]. Prior studies established that the hydrogen underpotential deposition (H_{upd}) peak directly reflects hydrogen binding energy (HBE), where more positive hydrogen desorption potentials correlate with stronger HBE [34]. As shown in Fig. 4(a), Mn/Pt-PtS displayed a negatively shifted H_{upd} peak compared to Pt-PtS and Pt/C, indicating weakened HBE that facilitated the Volmer step in alkaline HOR according to the bifunctional mechanism [2]. The CO stripping voltammetry test revealed OH adsorption capabilities, with more negative CO oxidation potentials signifying stronger OH_{ad} binding [34]. As depicted in Fig. 4(b), the CO stripping peak potential on Mn/Pt-PtS (0.72 eV) was smaller than that on Pt-PtS (0.79 eV) and Pt/C (0.75 eV). While zeta potential measurements (Fig. 4c) confirmed the enhanced surface negativity (−38.9 mV) of Mn/Pt-PtS relative to Pt-PtS (−18.7 mV). These collective results established the superior OH binding energy for Mn/Pt-PtS, with the hydroxyl binding energy (OHBE) hierarchy aligning precisely with alkaline HOR activity trends, confirming the strengthened kinetic benefits of OHBE for HOR catalysis [35,36]. As predicted, Mn/Pt-PtS maintained stable HOR current density in H_2-saturated electrolyte (1000 ppm CO), demonstrating that surface-bound hydroxyl species effectively oxidized the adsorbed CO intermediates to prevent catalytic poisoning (Fig. 4d). In contrast, under the same CO concentration, the current density of Pt/C drops sharply. This implies that the CO tolerance ability of Mn/Pt-PtS is quite admirable. To further assess the CO tolerance of the samples over time, we conducted chronoamperometric response curves [37]. After nearly 900 s of testing, the relative current retention rate of Mn/Pt-PtS significantly exceeded that of commercial Pt/C (Fig. 4g). This further confirmed the excellent CO tolerance of Mn/Pt-PtS, surpassing most catalysts reported in the literature (Table S5).

To further explore the CO tolerance mechanism of the catalyst, we performed in situ CO adsorption SEIRAS in 0.1 M KOH. CO

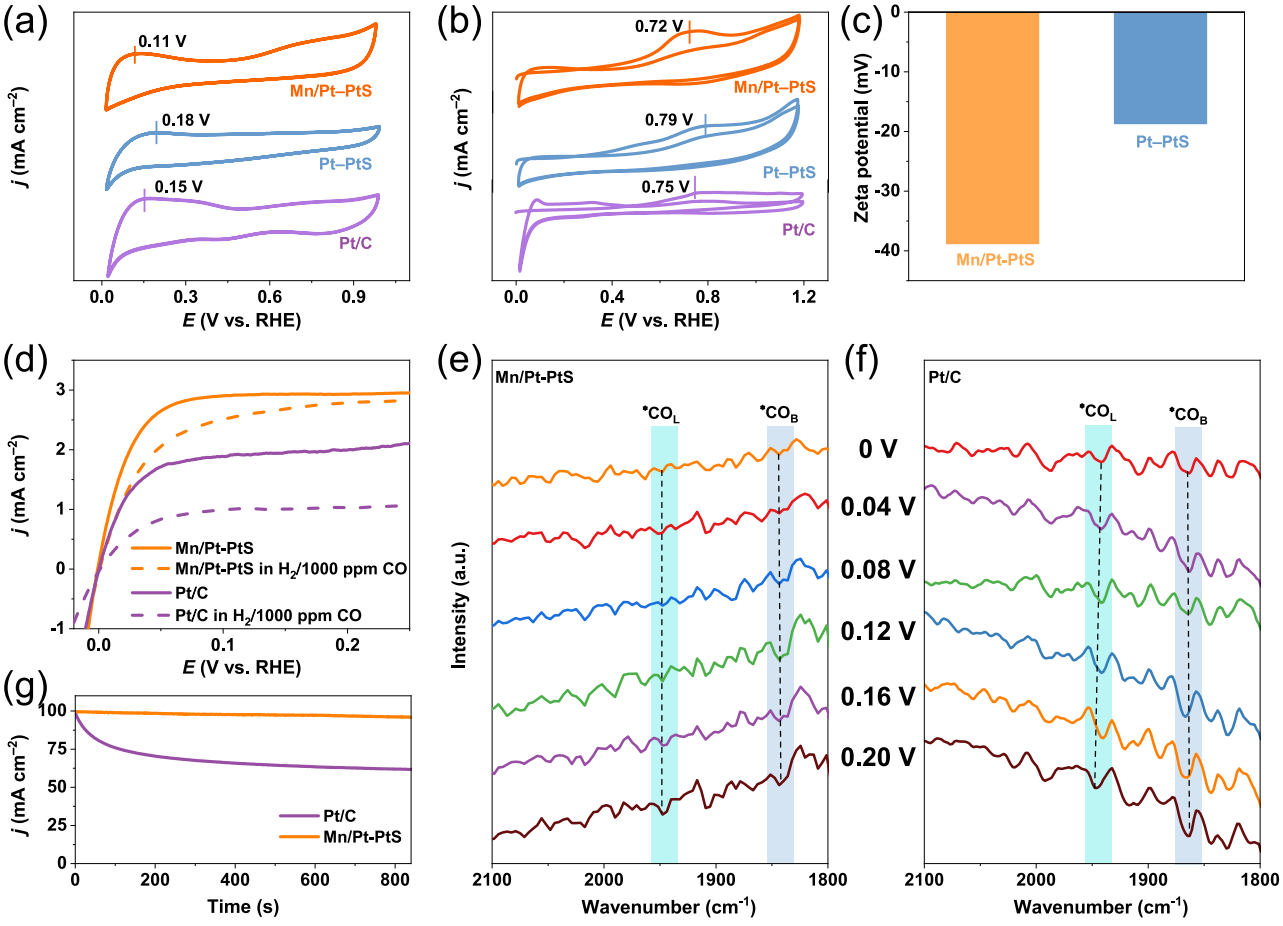

Fig. 4. (a) CV curves in N_2-saturated 0.1 M KOH at a scan rate of 50 mV s^{-1}. (b) CO stripping curves of Mn/Pt-PtS, Pt-PtS, and Pt/C. (c) Zeta potentials of Mn/Pt-PtS and Pt-PtS. (d) Polarization curves of Mn/Pt-PtS and Pt/C in 1000 ppm CO/H_2-saturated 0.1 M KOH. In situ SEIRAS depicting the CO adsorption state of (e) Mn/Pt-PtS and (f) Pt/C. (g) Chronoamperometry (*j*-*t*) response at 50 mV in H_2/1000 ppm CO-saturated 0.1 M KOH.

adsorption on the catalyst can be categorized into two types based on different adsorption states: bridge adsorption ($*CO_B$) around 1850 cm^{-1} and linear adsorption ($*CO_L$) around 1950 cm^{-1}, with $*CO_L$ being the cause of catalyst poisoning [38]. As seen from Fig. 4(e, f), compared with Pt/C, the peak intensities of $*CO_B$ and $*CO_L$ in Mn/Pt-PtS were significantly reduced, indicating a lower CO coverage on its surface. This indirectly mitigates its weaker CO adsorption, further explaining the strong CO poisoning resistance of Mn/Pt-PtS.

To elucidate the fundamental enhancement mechanism, in situ ATR-SEIRAS was employed to probe the structural evolution of interfacial water. As shown in Fig. 5(a, b), the ν_{O-H} band could be fitted into three peaks. The peak at the highest frequency was assigned to water molecules in the gap region, the peak at the lowest frequency was assigned to water molecules closest to the electrode, and the peak at the intermediate frequency was assigned to water molecules above the gap region [39]. It has been reported that water molecules in the gap region are closely associated with the hydrogen-bond network [13,40,41]. The proportions of water molecules in different gap regions for the obtained catalysts are shown in Fig. 5(c). As expected, the proportion of H_2O_{gap} in Mn/Pt-PtS was higher than that in Pt-PtS, indicating that the electronic modulation by Mn enabled the connectivity of the hydrogen-bond network in Mn/Pt-PtS to be greater than that in Pt-PtS, thus exhibiting the optimal catalytic activity for the oxygen reduction reaction [39,42–44]. Additionally, Fig. 5(d) shows that a redshift occurred in Mn/Pt-PtS, further indicating that more hydrogen bonds were formed between water molecules [39].

3.4. Theoretical study

To theoretically elucidate the catalytic origin of Mn/Pt-PtS for HOR, DFT calculations were systematically performed. Structural models of Mn/Pt-PtS and Pt-PtS were meticulously constructed for comparative analysis (Fig. S16). Charge-density distribution in Fig. 6(a) revealed pronounced electron depletion at Pt edges coupled with electron accumulation around Mn atoms, demonstrating strong interfacial electronic coupling between Mn and Pt constituents. Density of states (DOS) analysis (Fig. 6b) identified enhanced electronic states near the Fermi level for Mn/Pt-PtS versus Pt-PtS, signifying increased electron occupation and mobility at critical energy levels that enhance electrical conductivity [1]. The *d*-band center theory provides critical insights into intermediate adsorption behavior [45]. As shown in Fig. 6(c), the *d*-band centers of Mn/Pt-PtS and Pt-PtS were −2.13 and −2.48 eV, respectively. This indicated that the introduction of Mn could drive the *d*-band center to move closer to the Fermi level, and such a structural change was beneficial for optimizing and enhancing the OHBE [46,47]. The HBE is considered an effective descriptor of HOR activity [48]. Compared to the −0.37 eV of Pt-PtS, the introduction of Mn led to an optimal HBE of −0.28 eV for Mn/Pt-PtS, which was closer to the ideal zero Gibbs free energy, indicating a favorable HOR process (Fig. 6d and Fig. S17) [1,2]. Additionally, the adsorption of hydroxyl groups also affects the alkaline HOR, and the OHBE was calculated (Fig. 6e and Fig. S18). The OHBE values for Mn/Pt-PtS and Pt-PtS were −0.36 and −0.22 eV, respectively, indicating that Mn/Pt-PtS possessed a stronger OH binding energy, which aided in the removal of adsorbed CO and enhanced resistance to CO poisoning [49]. To further elucidate the fundamental causes of CO tolerance, CO adsorption energies were calculated (Fig. 6f and Fig. S19). The CO adsorption energy for Mn/Pt-PtS was significantly reduced to −0.13 eV compared to −0.24 eV for Pt-PtS, suggesting improved resistance to CO poisoning in Mn/Pt-PtS [5,50]. Moreover, we evaluated the energy profiles of Mn/Pt-PtS and Pt-PtS during the alkaline HOR process (Fig. 6g). As anticipated, the energy barrier for the water formation step in Mn/Pt-PtS (0.45 eV) was considerably lower than that of Pt-PtS (0.67 eV), further validating that the incorporation of the oxyphilic element Mn effectively enhanced the alkaline HOR kinetics [10,39,43]. Thus, the results indicated that Mn/Pt-PtS exhibited the optimal HBE and OHBE, leading to an enhanced HOR thermodynamics. Fig. 6(h) illustrates the HOR catalytic mechanism on the Mn/Pt-PtS model, providing a clearer understanding of the reaction process.

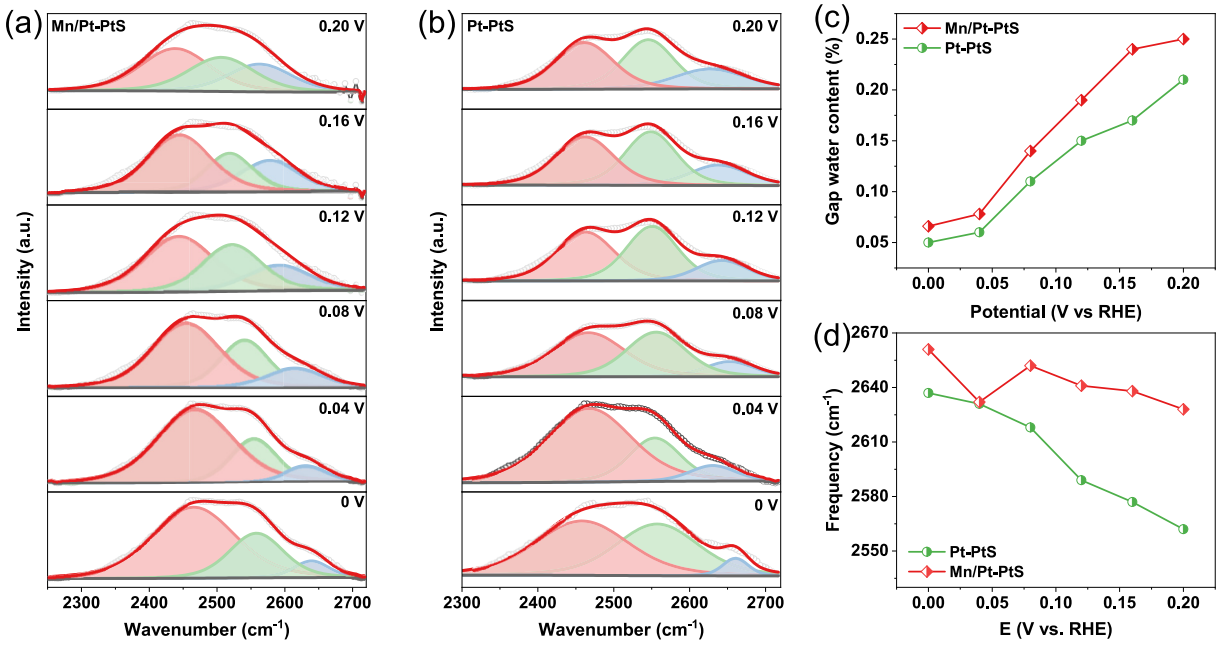

Fig. 5. (a, b) Deconvolution of the OH stretching vibration peaks at potentials from 0 to 0.2 V for Mn/Pt-PtS and Pt-PtS catalysts in H_2-saturated 0.1 M KOH solution. (c) Potential-dependent proportion of interfacial water from in situ SEIRAS spectra. (d) Comparison of the O–H stretching vibration frequencies of H_2O_{gap} of Mn/Pt-PtS and Pt-PtS.

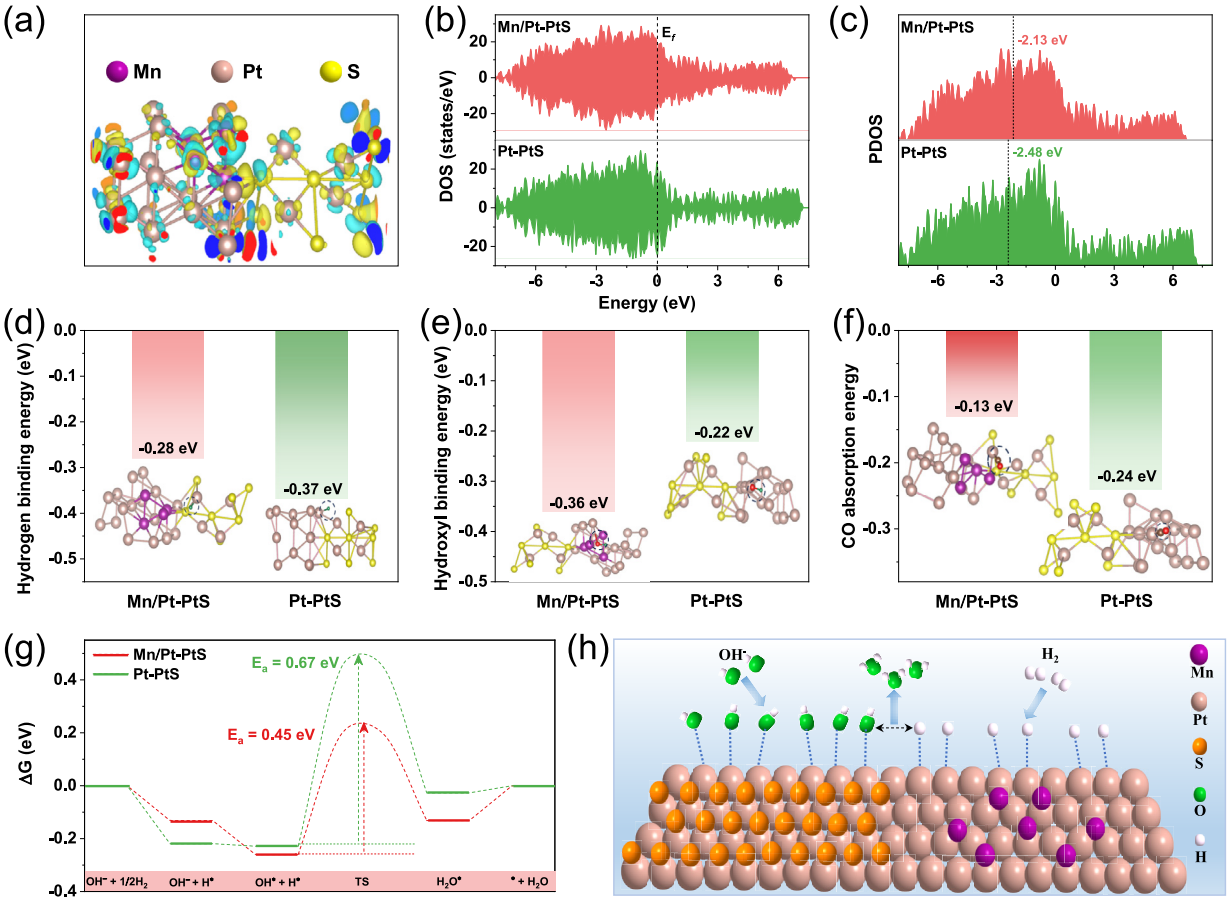

Fig. 6. (a) Local charge density of the Mn/Pt-PtS model. (b) The DOS plots. (c) The PDOS and *d*-band center value of Pt in Mn/Pt-PtS and Pt-PtS. (d–f) Calculated HBEs, OHBEs, and CO absorption energies on Mn/Pt-PtS and Pt-PtS models. (g) Gibbs free energy profiles of basic HOR on the surfaces of Mn/Pt-PtS and Pt-PtS. (h) Schematic illustration of the basic HOR mechanism on Mn/Pt-PtS.

4. Conclusions

In summary, by utilizing the oxophilic metal Mn to regulate the electronic structure of the catalyst, we successfully developed a high-performance Mn/Pt-PtS catalyst with a linear structure composed of stacked nanoparticles. The unique topological design confers Mn/Pt-PtS with expanded specific surface area and abundant coordinatively unsaturated active sites. The as-prepared Mn/Pt-PtS catalyst exhibited excellent HOR catalytic performance. Notably, Mn/Pt-PtS demonstrates robust operational durability and outstanding CO-poisoning resistance. Spectroscopic analyses coupled with theoretical analyses indicated that these performance enhancements originated from Mn-induced charge redistribution, which drives an upward shift in the *d*-band center to optimize hydrogen/hydroxyl adsorption energetics. Further analysis via in situ ATR-SEIRAS revealed the critical role of manganese in the restructured interfacial water, which promoted the connectivity of hydrogen bond networks. This investigation not only highlights the transformative potential of oxyphilic-element-mediated electronic modulation but also establishes hydrogen-bond network engineering as a pivotal strategy for HOR catalysis optimization, thereby establishing innovative paradigms for rational design of next-generation electrocatalysts.

CRediT authorship contribution statement

Chenggong Niu: Writing – original draft, Conceptualization. **Linyu Chen:** Methodology. **Yi Liu:** Investigation. **Shuqing Zhou:** Data curation. **Heyang Liu:** Data curation. **Tingting Tang:** Data curation. **Jingya Guo:** Writing – review & editing. **Tayirjan Taylor Isimjan:** Writing – review & editing. **Xiulin Yang:** Writing – review & editing, Supervision, Funding acquisition.

Declaration of competing interest

The authors declare that they have no known competing financial interests or personal relationships that could have appeared to influence the work reported in this paper.

Acknowledgments

This work has been supported by the National Natural Science Foundation of China (No. 52363028, 21965005), the Natural Science Foundation of Guangxi Province (2021GXNSFAA076001, 2018GXNSFAA294077), and the Guangxi Technology Base and Talent Subject (GUIKE AD23023004, GUIKE AD20297039).

Appendix A. Supplementary material

Supplementary material to this article can be found online at https://doi.org/10.1016/j.jechem.2025.07.070.

References

[1] Y. Liu, L. Cheng, S. Zhou, C. Niu, T.T. Isimjan, X. Yang, Appl. Catal. B Environ. Energy 362 (2025) 124709.

[2] J.-T. Ren, L. Chen, H.-Y. Wang, Y. Feng, Z.-Y. Yuan, Energy Environ. Sci. 17 (2024) 3960–4009.
[3] J. Park, H. Kim, S. Kim, S.Y. Yi, H. Min, D. Choi, S. Lee, J. Kim, J. Lee, Adv. Mater. 36 (2024) 2308899.
[4] Y. Liu, L. Cheng, S. Zhou, Y. Yang, C. Niu, T.T. Isimjan, B. Wang, X. Yang, J. Energy Chem. 94 (2024) 332–339.
[5] B. Cai, D. Shen, Y. Xie, H. Yan, Y. Wang, X. Chen, L. Wang, H. Fu, J. Am. Chem. Soc. 146 (2024) 33193–33203.
[6] J. Lin, Z. Zhang, J. Qiu, Y. Wu, J. Yu, Y. Li, X. Ren, L. Zhang, Z. Song, Chem. Eng. J. 506 (2025) 160156.
[7] Y. Gao, B. Ouyang, Y. Shen, W. Wen, J. Wang, M. Wang, Y. Sun, K. Xu, Adv. Energy Mater. 15 (2025) 2406114.
[8] H.-R. Pan, Z.-Q. Shi, X.-Z. Liu, S. Jin, J. Fu, L. Ding, S.-Q. Wang, J. Li, L. Zhang, D. Su, C. Ling, Y. Huang, C. Xu, T. Tang, J.-S. Hu, Angew. Chem. Int. Ed. 63 (2024) e202409763.
[9] W. Chen, J. Cao, J. Yang, Y. Cao, H. Zhang, Z. Jiang, J. Zhang, G. Qian, X. Zhou, D. Chen, W. Yuan, X. Duan, Nat. Commun. 12 (2021) 6888.
[10] X. Wang, X. Yin, P. Sun, L. Tang, Y. Tong, X. Li, X. Gao, X. Chen, X. Ma, Chem. Eng. J. 498 (2024) 155556.
[11] X. Zhao, H. Zhang, Y. Yan, J. Cao, X. Li, S. Zhou, Z. Peng, J. Zeng, Angew. Chem. Int. Ed. 56 (2017) 328–332.
[12] H. Wang, Y. Liang, S. Liu, X. Mu, H. Yu, K. Deng, Z. Wang, Y. Xu, L. Wang, Inorg. Chem. Front. 10 (2023) 5686–5693.
[13] Y. Jin, X. Fan, W. Cheng, Y. Zhou, L. Xiao, W. Luo, Angew. Chem. Int. Ed. 63 (2024) e202406888.
[14] Z. Huang, S. Hu, M. Sun, Y. Xu, S. Liu, R. Ren, L. Zhuang, T.-S. Chan, Z. Hu, T. Ding, J. Zhou, L. Liu, M. Wang, Y.-C. Huang, N. Tian, L. Bu, B. Huang, X. Huang, Nat. Commun. 15 (2024) 1097.
[15] T. Tang, W.-J. Jiang, S. Niu, N. Liu, H. Luo, Y.-Y. Chen, S.-F. Jin, F. Gao, L.-J. Wan, J.-S. Hu, J. Am. Chem. Soc. 139 (2017) 8320–8328.
[16] J. Bae, D. Shin, H. Jeong, C. Choe, Y. Choi, J.W. Han, H. Lee, ACS Catal. 11 (2021) 11066–11074.
[17] H. Huang, K. Liu, F. Yang, J. Cai, S. Wang, W. Chen, Q. Wang, L. Fu, Z. Xie, S. Xie, Angew. Chem. Int. Ed. 135 (2023) e202315752.
[18] X. Zhang, X. Fang, K. Zhu, W. Yuan, T. Jiang, H. Xue, J. Tian, J. Power Sources 520 (2022) 230882.
[19] V. Jose, H. Hu, E. Edison, W. Manalastas Jr., H. Ren, P. Kidkhunthod, S. Sreejith, A. Jayakumar, J.M.V. Nsanzimana, M. Srinivasan, J. Choi, J.-M. Lee, Small Methods 5 (2021) 2000751.
[20] L. Peng, C.-T. Hung, S. Wang, X. Zhang, X. Zhu, Z. Zhao, C. Wang, Y. Tang, W. Li, D. Zhao, J. Am. Chem. Soc. 141 (2019) 7073–7080.
[21] C. Yang, J. Yue, G. Wang, W. Luo, Angew. Chem. Int. Ed. 63 (2024) e202401453.
[22] X. Yang, L. Lin, X. Guo, S. Zhang, Small 20 (2024) 2404000.
[23] X. Yang, J. Liang, Q. Shi, M.J. Zachman, S. Kabir, J. Liang, J. Zhu, B. Slenker, M. Pupucevski, N. Macauley, A.J. Kropf, H. Zeng, D. Strasser, D.J. Myers, H. Xu, Z. Zeng, Y. Yan, G. Wu, Adv. Energy Mater. 14 (2024) 2400029.
[24] H. Wang, X. Qiu, W. Wang, L. Jiang, H. Liu, Front. Chem. 7 (2019) 855.
[25] X. Li, Z. Kou, S. Xi, W. Zang, T. Yang, L. Zhang, J. Wang, Nano Energy 78 (2020) 105230.
[26] J.T. Yu, S.S. Lin, Y.S. Huang, J. Appl. Phys. 65 (1989) 4230–4233.
[27] L. Gong, J. Zhu, F. Xia, Y. Zhang, W. Shi, L. Chen, J. Yu, J. Wu, S. Mu, ACS Catal. 13 (2023) 4012–4020.
[28] Y. Song, M. Sun, S. Zhang, X. Zhang, P. Yi, J. Liu, B. Huang, M. Huang, L. Zhang, Adv. Funct. Mater. 33 (2023) 2214081.
[29] Y. Liu, L. Cheng, S. Zhou, C. Niu, T. Taylor Isimjan, X. Yang, J. Colloid Interface Sci. 677 (2025) 997–1004.
[30] L. Zhang, S. Chen, T. Du, X. Zhao, A. Dong, L. Zhang, T. Li, L. Li, C. Yan, T. Qian, ACS Nano 18 (2024) 34195–34206.
[31] Y. Bao, M. Zha, P. Sun, G. Hu, L. Feng, J. Energy Chem. 59 (2021) 748–754.
[32] L. Wang, Z. Xu, C.H. Kuo, J. Peng, F. Hu, L. Li, H.Y. Chen, J. Wang, S. Peng, Angew. Chem. Int. Ed. 62 (2023) e202311937.
[33] H. Luo, K. Wang, F. Lin, F. Lv, J. Zhou, W. Zhang, D. Wang, W. Zhang, Q. Zhang, L. Gu, M. Luo, S. Guo, Adv. Mater. 35 (2023) 2211854.
[34] Y. Cong, F. Meng, H. Wang, D. Dou, Q. Zhao, C. Li, N. Zhang, J. Tian, J. Energy Chem. 83 (2023) 255–263.
[35] X. Zhang, L. Xia, G. Zhao, B. Zhang, Y. Chen, J. Chen, M. Gao, Y. Jiang, Y. Liu, H. Pan, W. Sun, Adv. Mater. 35 (2023) 2208821.
[36] L. Su, Y. Jin, D. Gong, X. Ge, W. Zhang, X. Fan, W. Luo, Angew. Chem. Int. Ed. 62 (2022) e202215585.
[37] S.-Z. Li, Z.-J. Lin, Q.-A. Chen, Z. Cai, Q. Li, J. Electrochem 30 (2024) 2404121.
[38] J. Yue, C. Yang, Y. Zhang, Q. Xiong, W. Luo, Chem. Sci. 16 (2025) 12096–12103.
[39] J. Yue, Y. Li, C. Yang, W. Luo, Angew. Chem. Int. Ed. 64 (2025) e202415447.
[40] P. Li, Y. Jiang, Y. Hu, Y. Men, Y. Liu, W. Cai, S. Chen, Nat. Catal. 5 (2022) 900–911.
[41] Y.-H. Wang, Y. Yang, F.-Y. Gao, X.-L. Zhang, L. Zhu, H.-K. Yan, P.-P. Yang, M.-R. Gao, Angew. Chem. Int. Ed. 63 (2024) e202407613.
[42] S. Li, L. Wu, Q. Liu, M. Zhu, Z. Li, C. Wang, X. Jiang, J. Li, J. Am. Chem. Soc. 145 (2023) 26711–26719.
[43] Y. Men, Y. Tan, P. Li, Y. Jiang, L. Li, X. Su, X. Men, X. Sun, S. Chen, W. Luo, Angew. Chem. Int. Ed. 63 (2024) e202411341.
[44] Y. Jin, Z. Han, W. Luo, Adv. Funct. Mater. (2025). https://doi.org/10.1002/adfm.202501377.
[45] P. Han, L. Wu, Y. Zhang, J. Yue, Y. Jin, H. Jia, W. Luo, Angew. Chem. Int. Ed. 64 (2025) e202419320.
[46] B. Hammer, J.K. Nørskov, Surf. Sci. 343 (1995) 211–220.
[47] Q. Hu, K. Gao, X. Wang, H. Zheng, J. Cao, L. Mi, Q. Huo, H. Yang, J. Liu, C. He, Nat. Commun. 13 (2022) 3958.
[48] J. He, L. Zeng, J. Li, D. Zhu, T. Gao, Y. Wang, Y. Chen, Nano Energy 128 (2024) 109894.
[49] F. Zhou, X. Ke, Y. Chen, M. Zhao, Y. Yang, Y. Dong, C. Zou, X.A. Chen, H. Jin, L. Zhang, S. Wang, J. Energy Chem. 88 (2024) 513–520.
[50] C. Yang, G. Wang, J. Yue, Z. Dai, W. Luo, ACS Catal. 15 (2025) 869–876.